Quantifying Neurite Growth Mediated by Interactions among Secretory Vesicles, Microtubules, and Actin Networks

Krasimira Tsaneva-Atanasova,[†] Andrea Burgo,[‡] Thierry Galli,[‡] and David Holcman[§*]

[†]Department of Computational Biology, Paris, France; [‡]INSERM Avenir Team, Membrane Traffic in Neuronal Epithelial Morphogenesis, Paris, France, and Institute Jacques Monod, Centre National de la Recherche Scientifique, UMR7592, Université Pierre et Marie Curie-Paris 6, Paris, France, and Université Denis Diderot-Paris 7, Paris, France; and [§]Department of Applied Mathematics, Weizmann Institute of Science, Rehovot, Israel, and Department of Computational Biology, Paris, France

ABSTRACT Neurite growth is a fundamental process of neuronal development, which requires both membrane expansions by exocytosis and cytoskeletal dynamics. However, the specific contribution of these processes has not been yet assessed quantitatively. To study and quantify the growth process, we construct a biophysical model in which we relate the overall neurite outgrowth rate to the vesicle dynamics. By considering the complex motion of vesicles in the cell soma, we demonstrate from biophysical consideration that the main step of finding the neurite initiation site relies mainly on a two-dimensional diffusion/sequestration/fusion at the cell surface and we obtain a novel formula for the flux of vesicles at the neurite base. In the absence of microtubules, we show that a nascent neurite initiated by vesicular delivery can only reach a small length. By adding the microtubule dynamics to the secretory pathway and using stochastic analysis and simulations, we study the complex dynamics of neurite growth. Within this model, depending on the coupling parameter between the microtubules and the neurite, we find different regimes of growth, which describe dendritic and axonal growth. To validate one aspect of our model, we demonstrate that the experimental flux of TI-VAMP but not Synaptobrevin 2 vesicles contributes to the neurite growth. We conclude that although vesicles can be generated randomly in the cell body, the search for the neurite position using the microtubule network and diffusion is quite fast. Furthermore, when the TI-VAMP vesicular flow is large enough, the interactions between the microtubule bundle and the neurite control the growth process. In addition, all of these processes intimately cooperate to mediate the various modes of neurite growth: the model predicts three different growing modes including, in addition to the stable axonal growth and the stochastic dendritic growth, a fast oscillatory regime. Finally our study demonstrates that cytoskeletal dynamics is necessary to generate long protrusion, while vesicular delivery alone can only generate small neurite.

INTRODUCTION

Neurite growth is a fundamental process in the generation of dendritic trees and axons leading to neuronal wiring during early brain development, learning, and regeneration. Axonal and dendritic genesis involves many cellular mechanisms, but the underlying specific rules are still unclear. Actin cytoskeleton and microtubules play a crucial role in neurite growth (1) and recent studies suggest that microtubules and actin microfilaments are anchored in a complex and regulated manner in the peripheral region of neuronal growth cones (2–4). Further, membrane addition through exocytosis is also required in the growth process (5), probably as early as in the nascent axon. Transport of new components to the plasma membrane is crucial for the expression of newly synthesized plasma membrane proteins such as adhesion molecules, growth factor receptors, and other proteins and lipids necessary for membrane expansion, motility of neuronal precursors, neurite outgrowth, and target recognition. In addition, recycling of these proteins plays a role in controlling their density at the plasma membrane and may be involved in vectorial membrane traffic during neurite outgrowth (6,7). The specific role of membrane traffic in the development and differentiation of neurons is only scarcely known and the molecular connections between vesicles and the cytoskeleton in neurites are only starting to be identified. Recently it has been demonstrated that membrane vesicles are delivered at the growing hyphal tip of the model fungus *Aspergillus nidulans* (8), a system that shares high similarities with neurite growth.

The lack of sensitivity of neurite growth to tetanus neurotoxin (9) and the normal neurite growth in mice deficient for the vesicular SNARE protein Synaptobrevin 2 (Syb2) suggest that Syb2 is not involved in neurite growth (10). Altogether, these results indicate that in coordination with actin dynamics, TI-VAMP plays a central role in neuritogenesis. At this stage, no experimental approaches were able to identify and quantify the respective contributions of microtubules, exocytosis and endocytosis, in neurite growth.

By constructing a biophysical model, we study the growth process and specifically relate the neurite outgrowth rate to the vesicular flux. In contrast to previous studies on neurite growth (11–22), we specifically base our analysis on the dynamics of secretory vesicles. In particular, we use the finding that membrane transport, as described previously is mainly mediated by a class of vesicles such as those

Submitted May 30, 2008, and accepted for publication October 21, 2008.

Krasimira Tsaneva-Atanasova and Andrea Burgo contributed equally to this work.

*Correspondence: holcman@biologie.ens.fr

Krasimira Tsaneva-Atanasova's present address is Department of Engineering Mathematics, University of Bristol, Bristol BS8 1TR, UK.

Editor: Marileen Dogterom.

0006-3495/09/02/0840/18 $2.00

doi: 10.1016/j.bpj.2008.10.036

characterized by the v-SNARE TI-VAMP (23,24): by fusing with the cell membrane, these vesicles deliver their membrane, which increases the surface area of the neurite (5,23,25–28). Microtubules also contribute to the neurite growth process by first being involved in vesicular trafficking (29–32), and second by stabilizing the neurite structure (33,34). We incorporate these findings in a model to study how the complex interactions of vesicles and microtubules lead to various growing regimes. Contrary to previous mathematical models of neurite growth (11–22), by changing the coupling parameter defining the interaction between microtubules and neurite, our model allows us to identify three type of neurite growth regimes, including axonal and dendritic growth (1,35,36) and a new oscillatory mode.

THEORY

Rate of vesicles fusion and neurite growth

We model the nonspecialized neuronal cell as a domain Ω, which can be approximated as a sphere of radius R. Vesicles are generated uniformly inside the cell body and their movement can be seen as alternating between a pure Brownian and a deterministic movement along microtubules. We assume for simplicity that microtubules emerge from the center of the cell and are organized radially and symmetrically, ending at the cell surface. The sites where neurites are initiated may correspond to preferential sites of exocytosis such as marked by the exocytosis complex (31,37) and/or determined by the location of the centrosome (1,38).

Our model of neurite growth starts with the delivery and insertion of vesicles at only few specific boundary locations, denoted by $\partial\Omega_a$ (29–31,39–41), which are, for example, the ones where the axon and the dendrites will be generated. Although vesicles may have different sizes, we only consider vesicles of a mean radius a. Because there are plenty of vesicles in the cytoplasm (hundreds to thousands), we neglect here the fluctuation in their number and consider that after a vesicle fuses, another is generated resulting in constant supply of new vesicles. This consideration allows us to keep the number of vesicles constant.

In our model, the growth is initiated by vesicles fusion (39) with the surface membrane: each time it happens, the vesicular membrane is used to increase the length of the neurite of a quantity l_0. For a cylindrical neurite of radius R_d, which does not change with vesicular fusion, the quantal increase l_0 of the total neurite length is given by

$$l_0 = \frac{2a^2}{R_d}. \tag{1}$$

The dynamics of the neurite is also controlled by the membrane endocytosis rate k_2. When the neurite radius does not change, the endocytosis rate is proportional to the neurite surface.

To estimate the growth rate, we evaluate the flux of vesicles to the initial neurite location $\partial\Omega_a$ and use the narrow escape theory, described in Holcman and Schuss (42). In this theory, we computed the mean time a Brownian particle takes to arrive at a small absorbing surface $\partial\Omega_a$ while at the remaining boundary the particle is reflected. We approximate a vesicle as a round homogeneous sphere and thus its free movement is modeled here by the overdamped limit of the Langevin equation (43). Furthermore, because a vesicle can also bind and then drift along microtubules with a deterministic velocity, its global motion is described by the stochastic rule

$$\dot{X} = \begin{cases} \sqrt{2D}\dot{w} & \text{for } X(t) \text{ free} \\ V(t)\mathbf{r} & \text{for } X(t) \text{ bound} \end{cases}, \tag{2}$$

where $X(t)$ denotes the position and $V(t) \geq 0$ is a time-dependent drift velocity along microtubules directed toward the cell surface. For simplicity, we assume that the velocity along the microtubules is constant, w is a δ-correlated standard white noise, and $\mathbf{r}$ is the radial unit vector. To obtain an explicit expression for the vesicular flux to the neurite initiation, we replace the vesicles dynamics given in Eq. 2 with a stochastic equation containing a steady-state drift $\phi(\mathbf{X})$,

$$\dot{\mathbf{X}} = \nabla\phi(\mathbf{X}) + \sqrt{2D}\dot{\boldsymbol{\omega}}, \tag{3}$$

where ϕ is the potential per unit mass, which generates the flow field velocity given by $\phi(\mathbf{X}) = \vartheta r/\gamma$ and the diffusion constant is given by $D = k_B T_p/m\gamma$, m is the vesicle mass, γ is the viscosity coefficient, T_p is the temperature, and k_B is Boltzmann's constant. To validate the procedure, which consists of replacing Eq. 2 by Eq. 3, we choose the constant velocity field, ϑ, as described in Appendix 1, by first using an explicit solution of the associated Fokker-Planck equation (FPE) and then fitting it to the vesicles distribution generated by Brownian simulations of Eqs. 2 and 3. In these simulations, vesicles are moving inside a slice domain (Fig. 1) where the boundary associated with the dynamics of Eq. 2 (Fig. 1 *A*) represents the place where the drift occurs, while it is simply reflective in the case of Eq. 3 (Fig. 1 *B*). In Fig. 1 *A*, we show the histogram of vesicles distribution generated by the Brownian simulation of Eq. 2 with 1000 vesicles, which is then fitted using the solution of the FPE and by using the optimal amplitude velocity. Using the same drift amplitude, we generated the distribution of vesicles following Eq. 3 and as a control experiment, we fitted the histogram with the solution of the FPE, which turns out to be in very good agreement with our choice of ϑ (Fig. 1 *B*). For our simulations of vesicular diffusion and velocity along microtubules, we use parameter values obtained from experimental studies in PC12 cells (44,45) and *Xenopus* embryo neuronal cultures (32).

By using the distribution of vesicles at steady state, and the property that the surface of the neurite base (initiation

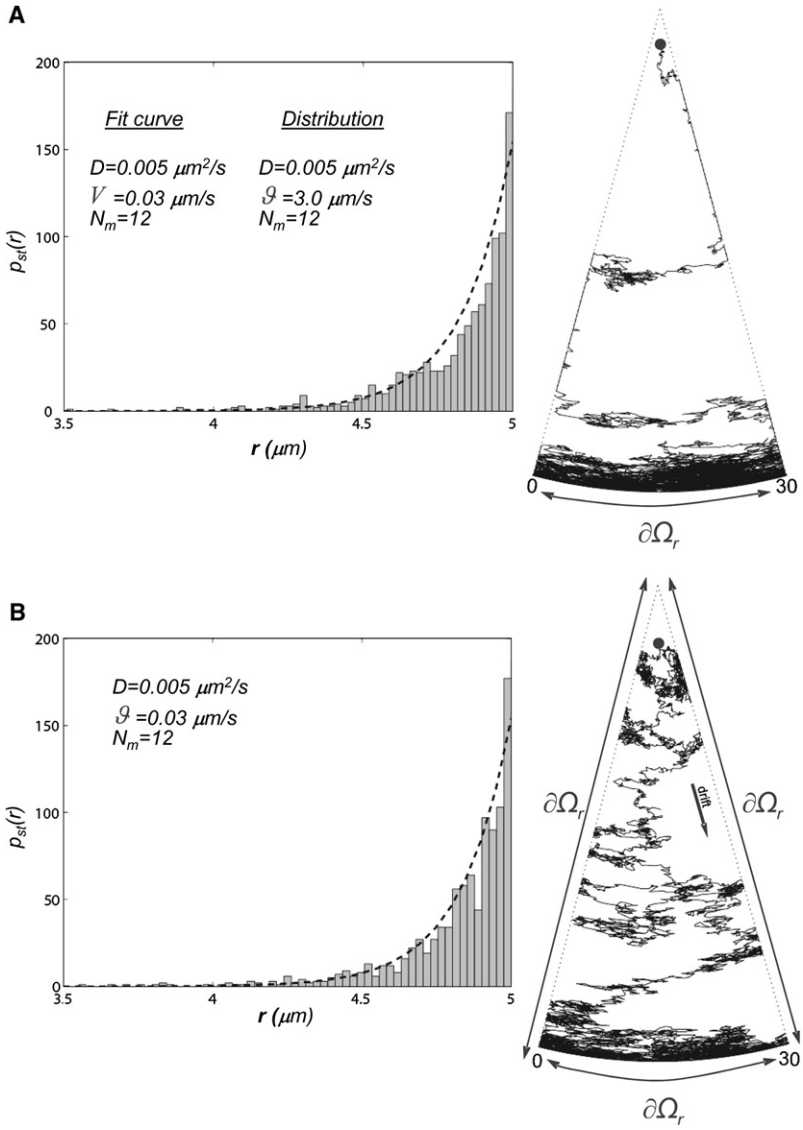

FIGURE 1 Plot of the steady-state distribution ($N_0 = 1000$) and the probability density function given by the Fokker-Planck equation. (*A*) Two-dimensional sample membrane vesicle trajectory obtained by simulating Eq. 2. (*B*) Two-dimensional sample membrane vesicle trajectory obtained by simulating Eq. 3.

site) is small compared to the rest of the soma area, we compute the flux of vesicles at the initial neurite surface $\partial\Omega_a$. We base this computation on the scenario that vesicles are confined to the cellular domain Ω, whose boundary $\partial\Omega$ is reflecting, except for a small absorbing window $\partial\Omega_a$ ($\partial\Omega = \partial\Omega_a \cup \partial\Omega_r$). Each time a vesicle arrives to the area $\partial\Omega_a$, it is exocytosed and delivers its membrane. During this process, somewhere inside the cell, at the timescale considered, a new vesicle is instantly generated. In this way, we maintain the total number of vesicles constant. To determine the rate of vesicles arrival contributing to the neurite growth, we start with the probability density function (pdf) $p_\delta(\boldsymbol{x},t)$ of finding a vesicle at position $\boldsymbol{x}$ at time t, defined by

$$p_\delta(\boldsymbol{x},t|\boldsymbol{x}_0)d\boldsymbol{x} = Pr\{\boldsymbol{x}(t)\in\boldsymbol{x} + d\boldsymbol{x}|\boldsymbol{x}(0) = \boldsymbol{x}_0\}. \quad (4)$$

The pdf satisfies the forward equation (43)

$$\frac{\partial p_\delta}{\partial t} = D\Delta p_\delta - \nabla\cdot(p_\delta\nabla\phi), \quad (5)$$

with the mixed boundary conditions

$$p_\delta(\boldsymbol{x},t) = 0, \quad \text{for} \quad \boldsymbol{x}\in\partial\Omega_a \quad (6)$$

$$\boldsymbol{J}.\boldsymbol{n}(\boldsymbol{x},t) = 0, \quad \text{for} \quad \boldsymbol{x}\in\partial\Omega_r \quad (7)$$

and the initial condition

$$p_\delta(\boldsymbol{x},0) = p_0(\boldsymbol{x}). \quad (8)$$

Since $|\partial\Omega_a|$ is a small disk of radius δ, the average time a vesicle spends at $\boldsymbol{x}$ before arrival at the neurite initiation $|\partial\Omega_a|$ is defined as (43)

$$u_\delta(\boldsymbol{x}) = \int_0^\infty p_\delta(\boldsymbol{x},t)dt. \quad (9)$$

To derive an asymptotic estimate of $u_\delta(\boldsymbol{x})$, we base our analysis on the result presented in Singer and Schuss (46) and the rate of vesicles arrival is the reciprocal of the mean first passage time defined by the mean

$$\overline{\tau}_\delta = \int_\Omega u_\delta(\boldsymbol{x})d\boldsymbol{x} \approx \frac{e^{-\phi_0/D}}{4D\delta}\int_\Omega \exp\left\{\frac{\phi(\boldsymbol{x})}{D}\right\}d\boldsymbol{x}. \quad (10)$$

At this stage, the analysis differs from Singer and Schuss (46), since this drift is now directed toward the surface membrane. To estimate the integral using Eq. 10, we use the approximation that the diffusion D is much smaller than the drift (32,44,45) and thus by applying Laplace's method, we get

$$\int_\Omega \exp\left\{\frac{\phi(\boldsymbol{x})}{D}\right\}d\boldsymbol{x} \approx D\exp\left\{\frac{\phi_m}{D}\right\}\int_{\partial\Omega}\frac{dS_\theta}{\frac{\partial\phi}{\partial r}(0,\theta)} + o(D), \quad (11)$$

where ϕ_m the global maximum of ϕ, which is achieved everywhere on the reflecting boundary $\partial\Omega_r$. In the case of a radial symmetrical cell, where Ω could be approximated by a sphere, we evaluate the above integral explicitly as

$$\int_\Omega \exp\left\{\frac{\phi(\boldsymbol{x})}{D}\right\}d\boldsymbol{x} = \frac{4\pi D}{\vartheta}\left[R^2 - \frac{RD}{\vartheta} + \frac{D^2}{\vartheta}\right]\exp\left\{\frac{\phi_m}{D}\right\}, \quad (12)$$

and where $\vartheta = \partial\phi/\partial r$ is the constant drift along microtubules. Hence,

$$\overline{\tau}_\delta = \frac{\pi e^{\frac{\phi_m-\phi_0}{D}}}{\delta\vartheta}\left[R^2 - \frac{RD}{\vartheta} + \frac{D^2}{\vartheta}\right]. \quad (13)$$

Thus, we obtain that the vesicles arrival rate is given by

$$\kappa_\delta = \frac{1}{\overline{\tau}_\delta} = \frac{\delta\vartheta}{\pi\left[R^2 - \frac{RD}{\vartheta} + \frac{D^2}{\vartheta}\right]}e^{-\Delta E/D}, \quad (14)$$

where $\Delta E = \phi_m - \phi_0$. Since $\Delta E = 0$ (because ϕ_0 and ϕ_m are both achieved on the cell surface) and neglecting the contribution of the last two terms in the denominator (which is ~1%), we get

$$\kappa_\delta = \frac{1}{\overline{\tau}_\delta} \approx \frac{\delta\vartheta}{\pi R^2}. \quad (15)$$

To derive this formula, the reader should keep in mind that the switching dynamics of the vesicle described by Eq. 2 has been coarse-grained by a stochastic equation with a radial constant drift (Eq. 3). We describe this procedure in Appendix 1 and in Fig. 1, we plot the distributions of particles obtained from Eqs. 2 and 3, which agree reasonably well. Thus we conclude that the effective drift ϑ captures the microtubule organization. Furthermore under the spherical cell approximation, the maximum of the potential ϕ is achieved everywhere on the cell surface. Situations where ΔE is not zero may occur in nonspherical cells where the neurite initiation is located at a distance different from where the maximum of ϕ is achieved.

Markov equations of neurite growth

We now derive the master equation of the neurite growth: because vesicles arrive at random times at the neurite base, we complete the study of neurite length dynamics as follow: The neurite growth increases proportionally to the flux of vesicles and exocytosis, and decreases due to endocytosis that can happen anywhere on the neurite surface membrane (47). We also confirmed that fluid phase endocytosis occurs all along axons and dendrites of hippocampal neuron in primary culture (our unpublished observation). Exocytosis and endocytosis (characterized by a constant k_2) are both following a Poissonian distribution. The probabilities $p_q(t) = Pr\{L(t) = ql_0\}$ that at time t a neurite has exactly length ql_0 satisfies

$$\dot{p}_q(t) = -[k_2 q + \kappa_\delta N_0]p_q(t), \quad (16)$$

$$\begin{aligned}\dot{p}_0(t) = {} & -\kappa_\delta N_0 p_0(t) + k_2 p_1(t), \text{ for } q = 0,\\ & + k_2(q+1)p_{q+1}(t)\\ & + [\kappa_\delta N_0]p_{q-1}(t), \text{ for } q \geq 1,\end{aligned} \quad (17)$$

where q is quantal number, l_0 is quantal length given by a single vesicle fusion, and the total number of vesicles N_0 is maintained constant inside the soma. The mean and the variance of p_q are given by $M(t) = \sum_{q=1}^{\infty} qp_q(t)$, $\sigma^2(t) = \sum_{q=1}^{\infty} q^2 p_q(t) - M^2(t)$, and at steady state we get $M(\infty) = \kappa_\delta/k_2 N_0$ and $\sigma^2(\infty) = \kappa_\delta/k_2 N_0$.

Finally a standard analysis shows that the mean length of the neurite satisfies

$$\frac{dL}{dt} = l_0 N_0 \kappa_\delta - k_2 L. \quad (18)$$

When initially the neurite length is zero, by integrating Eq. 18, the time-dependent length is

$$L(t) = \frac{l_0 N_0 \kappa_\delta}{k_2}\left(1 - e^{-k_2 t}\right), \quad (19)$$

and at steady state

$$L_{eq} = \frac{l_0 N_0 \kappa_\delta}{k_2}. \quad (20)$$

For a time-dependent flux of vesicles given by $J(t)$, the neurite length satisfies the equation

$$\frac{dL}{dt} = J(t) - k_2 L. \quad (21)$$

METHODS

Numerical simulations

The computer simulations are performed using MATLAB (The MathWorks, Natick, MA). We model vesicles dynamics using the Smoluchowski limit of the Langevin equation. In the simulations, we generated the random motion of each vesicle as described by Eq. 3. This is an analog to a Monte Carlo type simulation. The differential equations associated with the neurite length and the equations for the microtubules bundle are simulated by a standard forward Euler scheme. The parameter values used in the numerical simulations are given in Table 1 and the figure legends.

TABLE 1 Parameter values of the model

Parameter	Value
D	0.005 $\mu m^2\ s^{-1}$
ϑ, ϑ_0	0.083 $\mu m\ s^{-1}$
k_a	0.42 $\mu m\ s^{-1}$
k_d	4.2 $\mu m\ s^{-1}$
R	5 μm
R_d	0.5 μm
δ	$R/60$ μm
N_0	6000
ϵ	0.01 μm
σ'_v	1
σ''_v	10

Description of the numerical simulations

In the numerical simulation of Fig. 1, the number of vesicles N_0 is maintained constant. The first type of simulations (Fig. 1 *A*) consists of running independent and noninteracting vesicles, described by the following rules:

Free. A vesicle diffuses freely inside the cytoplasm with a diffusion coefficient D.

Bound. When a vesicle is bound to a microtubule, we only consider the movement toward the cell surface. A vesicle is assumed attached to a microtubule if it is found at distance ≤ 10 nm away from it. We assume that each attached vesicle has a Poissonian probability of parameter 0.4 to be detached from the microtubule and to become free.

The histogram of the vesicles distribution is given in Fig. 1, where the simulation is performed in an angular domain, defined by the angle $\angle 30°$. We chose such a domain to save simulation time. The histogram of the vesicles distribution is then fitted by using the best choice of the drift amplitude in the solution of the FPE (see Appendix 1, Eq. 31), normalized such that

$$p_{sect}(r) = N_m p_{st}(r), \tag{22}$$

where $N_m = 12$ is the number of microtubules in a two-dimensional cell and p_{st} is given in Eq. 31. The simulations associated with Eq. 3 are obtained by using a standard Euler scheme for stochastic equations with reflecting boundary conditions (Fig. 1 *B*).

Cell culture and DNA constructs

PC12 cells were cultured in RPMI containing 10% horse serum (HS) and 5% fetal bovine serum and plated on collagen-coated glass coverslips as described previously (24). Chimera between red fluorescent protein (mRFP) and TI-VAMP was obtained by subcloning the cDNA encoding full-length rat brain TI-VAMP into the mRFP-C1 vector (provided by C. Gauthier-Rouviere, CRBM, Montpellier, France). EGFP-Syb2 was previously described.

Time-lapse imaging and fluorescence quantification analysis

PC12 cells were co-transfected with mRFP-TI-VAMP and EGFP-Syb2 using Lipofectamine 2000 Reagent (Invitrogen, Carlsbad, CA) according to the manufacturer's instructions. The onset of fast neuritogenesis was induced 24–48 h after the transfection by application of 100 nM staurosporine. Images used for monitoring the fluorescent protein (FP)-labeled vesicles were recorded every 60 s over a time period of 40–90 min by using an inverted microscope (Leica DMI6000B, Solms, Germany) equipped with 63×/1.4 Plan-Apochromat oil-immersion objectives and digital camera (Cascade:512B; Roper Scientific, Trenton, NJ). For dual-color imaging, channels were collected sequentially. Imaging was conducted in modified Krebs-Ringer-HEPES buffer (140 mM NaCl, 4.7 mM KCl, 2 mM MgCl, 0.5 mM CaCl, 10 mM HEPES, and 5.5 mM glucose, pH 7.4, with NaOH). Temperature was controlled by warmed air (37°C). Lamp power and exposure time were the lowest possible (10–30% Hg lamp, 100–200 ms) to avoid phototoxicity. Quantification of integrated fluorescence intensity was conducted independently for every FP-tagged protein by using the grid module of MetaMorph software. Briefly, after images were threshold, a grid mask was designed on the growing neurite, from the cell body limit to the maximum extent of the process, and segmented in seven equal stages. Integrated fluorescent intensity was collected from each stage and converted automatically in numerical data. Curves for the two FP-tagged proteins were generated for every stage, allowing us to compare their dynamics (see Fig. 7 for details). The experiments were repeated at least five times.

RESULTS

Modeling vesicles dynamics in the soma and estimation of the vesicular flux

Our model of neurite growth starts with the delivery and insertion of vesicles at a few specific boundary locations (Fig. 2 *A*). To estimate the neurite growth rate, we first evaluate the flux of vesicles to the initial neurite location. For that purpose, we approximate the motion of vesicles by the overdamped limit of the Langevin equation (43). Vesicles are generated inside the cell body and their movement can be seen as alternating between a pure Brownian motion and a deterministic movement along microtubules or actin

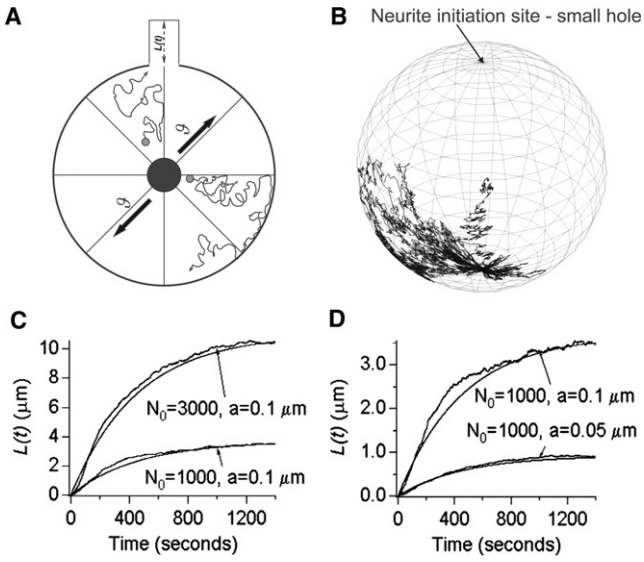

FIGURE 2 (*A*) Schematic representation of the vesicles dynamics in the cell body, giving rise to a newly formed protrusion at the neurite initiation site. (*B*) A sample membrane vesicle trajectory in a three-dimensional cell produced by simulations of the homogenized version of the model (Eq. 3). (*C*) Plot of the simulated neurite length from Eq. 3 superimposed onto the curve produced by the formula for the mean length given in Eq. 19 for two different vesicles numbers that are available in the soma and endocytosis rate—$k_2 = 0.0022\ s^{-1}$ (52,55). (*D*) Plot of the simulated neurite length from Eq. 3 superimposed onto the curve produced by the formula for the mean length given in Eq. 19 for two different vesicles radii and endocytosis rate—$k_2 = 0.0022\ s^{-1}$ (52,55).

filaments. The overall motion is described by the switching rule from Eq. 2. To obtain an explicit expression for the vesicular flux to the neurite initiation, we replace the vesicles dynamics given by Eq. 2 with a stochastic equation containing a steady-state drift as in Eq. 3. Vesicles are independent entities, confined to the cell cytoplasm, whose boundary is reflecting, except for the small neurite initiation surface (compared to the rest of the soma area) where vesicles are absorbed. The total number of vesicles inside the cell is large compared to the exocytosed vesicles that deliver their membrane to the neurite. Such dynamics requires that somewhere inside the cell, a new vesicle be generated almost instantly, which corresponds to constant supply of vesicles by Golgi. To determine the rate of vesicles arrival, we use the probability density function (pdf) $p_\delta(\boldsymbol{x},t)$ of finding a vesicle at position $\boldsymbol{x}$ at time t as in Eq. 4. The pdf satisfies Eq. 5 with reflecting boundary conditions from Eq. 6 except at the neurite initiation site (Eq. 7), where vesicles are absorbed (43). By solving Eq. 5 and using the small hole theory (48), we obtain a new formula that gives the arrival rate of vesicles to the neurite initiation (see Eq. 15) for uniformly distributed vesicles inside the cytoplasm. It is interesting to note that Eq. 15 agrees with the flux measured experimentally in Hill et al. (45). Indeed, using the parameters from Table 1, for a population of $N = 6000$ vesicles, we get a rate $N_0\kappa_\delta = 0.52$ vesicles/s, while the experimentally measured in PC12 cells value is estimated as ~0.5 vesicles/s (45). This excellent agreement shows that this biophysical scenario based on diffusion and MT-transport captures the main features of the early vesicular delivery. In addition, we have extended the delivery rate, given by Eq. 15, by taking into account the effects of possible environmental regulation of the vesicular flux rate (see Appendix 2).

Moreover, as suggested by the numerical simulations (Fig. 2 *B*), vesicles are first directed toward the surface where they are maintained dynamically as a result of the direct interaction with the microtubule or actin network (49). Close to the plasma membrane, the actin plays a similar role as the microtubule network and vesicle can now attach and detach to actin (4,8), which leads to a confined motion along the cell surface. It is interesting to note that as a result of the alternating epochs of diffusion and motion along microtubules toward the plasma membrane, vesicles explore the soma area before finding the neurite initiation site. This result is supported by the observations (30) that vesicles move along the cell surface before fusion. This is a sophisticated strategy since finding the neurite entrance is much faster by exploring the soma surface, which is two-dimensional, instead of moving randomly in the cytoplasm, which is three-dimensional (48). Fig. 2 *B* shows a Brownian simulation of a vesicle that moves near the surface before reaching the neurite initiation. It will be interesting to track vesicles experimentally and to estimate the flux at the neurite base.

Finally, each time a vesicle fuses with the surface membrane, the vesicular membrane is used to increase the length of the neurite of a quantity l_0 (Fig. 2 *A*). For a cylindrical neurite of radius R_d, which does not deform with vesicular fusion, the quantal increase of the total neurite length is given by Eq. 1. From the balance between an exocytosis rate $N_0\kappa_\delta$ and a membrane endocytosis rate k_2 (both rates are Poissonian), where vesicles can be endocytosed anywhere on the neurite surface membrane, we can derive the dynamics of the neurite outgrowth and the solution gives that the neurite length is determined by Eq. 19. The length at steady state is given by Eq. 20. At this stage, we conclude that all neurites sharing the same radius δ at the soma, have the same steady-state length, which is reminiscent of growth cone structure. The formula for L_{eq} predicts a short neurite length, which does not require any microtubules activity (39). In Fig. 2 *C*, we show the result of Brownian simulations where vesicles are exocytosed with Poissonian rate given by Eq. 15 and endocytosed with a constant rate k_2. We superimpose the stochastic neurite dynamics and the deterministic solution given by Eq. 19 for two values of the vesicles numbers 1000 and 3000. In Fig. 2 *D*, we compare the effect of the vesicles radius on the overall dynamics and we conclude that two different vesicles radii lead to two different steady-state neurite lengths. For a steady-state number of 3000 vesicles and a size of $a = 0.1$ μm, the steady mean length L_{eq} is equal to 10.6 μm, and is attained in ~20 min. Thus, in the absence of other regulatory mechanisms and for a fixed neurite radius, a fixed number of vesicles and for a given cell geometry, all emerging neurites reach the same steady-state length with a rate constant dictated by the endocytosis rate k_2. In this part of the model, which concerns short neurites, we neglected the vesicular transport to the neurite tip.

Modeling neurite elongation using microtubule-neurite interactions

To further investigate how neurites elongate, we now include the microtubule dynamics and its interaction with the neurite and vesicles. Indeed, we recall that microtubules can 1), direct vesicles to the cell periphery (29) inside the neurite (50) and 2), they can attach to the neurite tip in a complex interaction with actin microfilaments (2,4). Furthermore, when a microtubule bundle is attached to the neurite, both structures are stabilized (33,34,51,52), preventing them from a possible collapse.

To study the properties of the overall system, which consists of trafficking vesicles and a unique microtubule bundle, interacting with the growing neurite, we start the analysis when vesicles are delivered at the proximal end of the neurite (31,40). As computed above, vesicles arrive at a Poissonian rate κ_δ given by Eq. 15. We approximate the neurite geometry as a long and thin cylinder, where a schematic diagram of the model is presented in Fig. 3 *A*. We model the neurite tip as a narrow layer that accounts for the submembrane F-actin bundles, stabilizing the microtubules

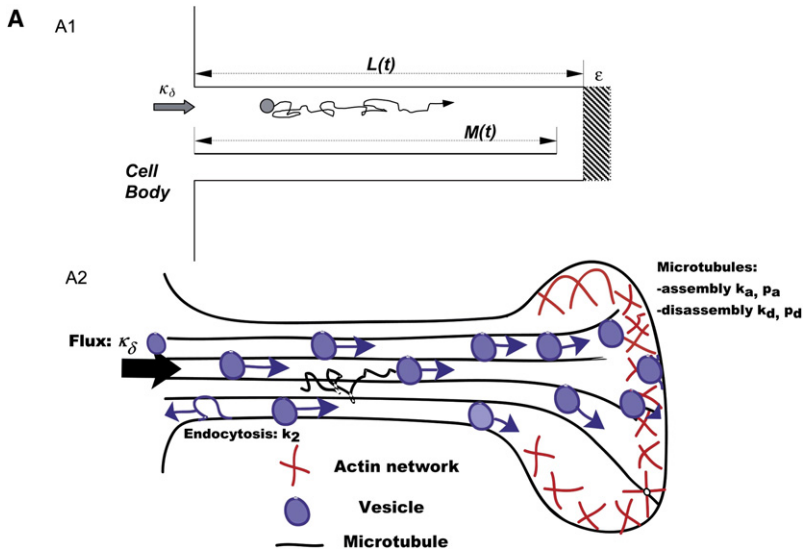

FIGURE 3 Schematic diagram of the neurite elongation model described by Eqs. 44–48.

attached to it (33,34). We approximate the vesicular motion (Appendix 3) as one-dimensional Brownian with a drift along microtubules. Vesicles move inside the neurite until they reach the distal neurite tip, where exocytosis occurs with a certain probability (27,31,32,40,53). At the neurite tip each fusing vesicle contributes length-of-magnitude l_0 (Eq. 1) to the total membrane surface of the neurite.

In our simulations, vesicles are injected at the soma/neurite interface at a Poissonian rate κ_δ and once inside the neurite, they move until fusion occurs at the neurite tip (53). Meanwhile, the microtubules bundle of length, $M(t)$, assembles at a Poissonian rate k_a with a probability p_a and disassembles at a rate k_d with a probability p_d (12,34,54). When the microtubules bundle end reaches the neurite tip, it can stabilize the actin network and both structures can interact by attaching together with a probability p_{att} (attachment probability). This attaching process accounts for the experimental observations (33,34) in which the state of F-actin in the neuronal growth cone regulates the growth rate. When attached to the F-actin, we consider that microtubules persistently grow at a rate governed by the vesicular exocytosis rate. This consideration is supported by the microtubule behavior during mitosis and in vitro studies with purified tubulin (54).

Microtubule dynamics depends on the assembly and disassembly rates, but it also depends on the concentration of tubulin inside the neurite. In our model, we neglected the tubulin dynamics and the interaction with other stabilizing signaling molecules. Our approach assumes a sufficient amount of free tubulin dimers and thus does not explicitly account for any changes in tubulin concentration inside the neurite. This assumption relies on fast equilibration of tubulin molecules, which diffuse much faster than the timescale at which the neurite grows. The tubulin concentration can thus be considered uniform in the neurite, in contrast to the growth cone, where tubulin concentration is expressed in gradients (18).

When the microtubules bundle reaches the neurite tip, both structures are stabilized and this coupling affects the endocytosis rate, which switches from a higher to a lower value. These rates measure the membrane vesicles endocytosis in the presence or in the absence of the microtubules bundle attached to the neurite. The decay of the endocytosis rate when the bundle is attached (as observed experimentally in neurons derived from chicken embryo (51,52)) corresponds to a stabilization mechanism (33,34). It is based on the idea that an attached bundle increases the minimal surface tension necessary to form a vesicle by endocytosis.

Finally, the neurite length increases proportionally to the flux of vesicles fusing at the tip of the neurite and decays due to vesicles endocytosis (see Appendix 3). Applying these rules, we show the results of stochastic simulations of neurite growth (Fig. 4). When we vary the probability p_a (equivalently p_d) for the microtubules assembly (disassembly), for a fixed endocytosis rate k_2 (Fig. 4 *A*) and a large number of vesicles, the neurite growth regime is dominated by the microtubules interacting with the neurite. The effect of increasing the endocytosis rate k_2 is presented in Fig. 4 *B* compared with Fig. 4 *A*. As shown by comparing these two panels, when we vary p_a/p_d, p_{att}, and k_2, we could identify three main regimes:

In the first regime (Fig. 4 *A*1), the microtubules bundle can collapse without leading to neurite collapse. This regime is equivalent to the simulation results shown in Fig. 2, *C* and *D*, and is characterized by a very weak coupling between the neurite and the microtubules bundle. Thus, it produces short neurites and can be correlated with experimental findings (39).

In a second regime, where the MT-bundle and the neurite are sufficiently coupled (Fig. 4, *A*2, *B*1, and

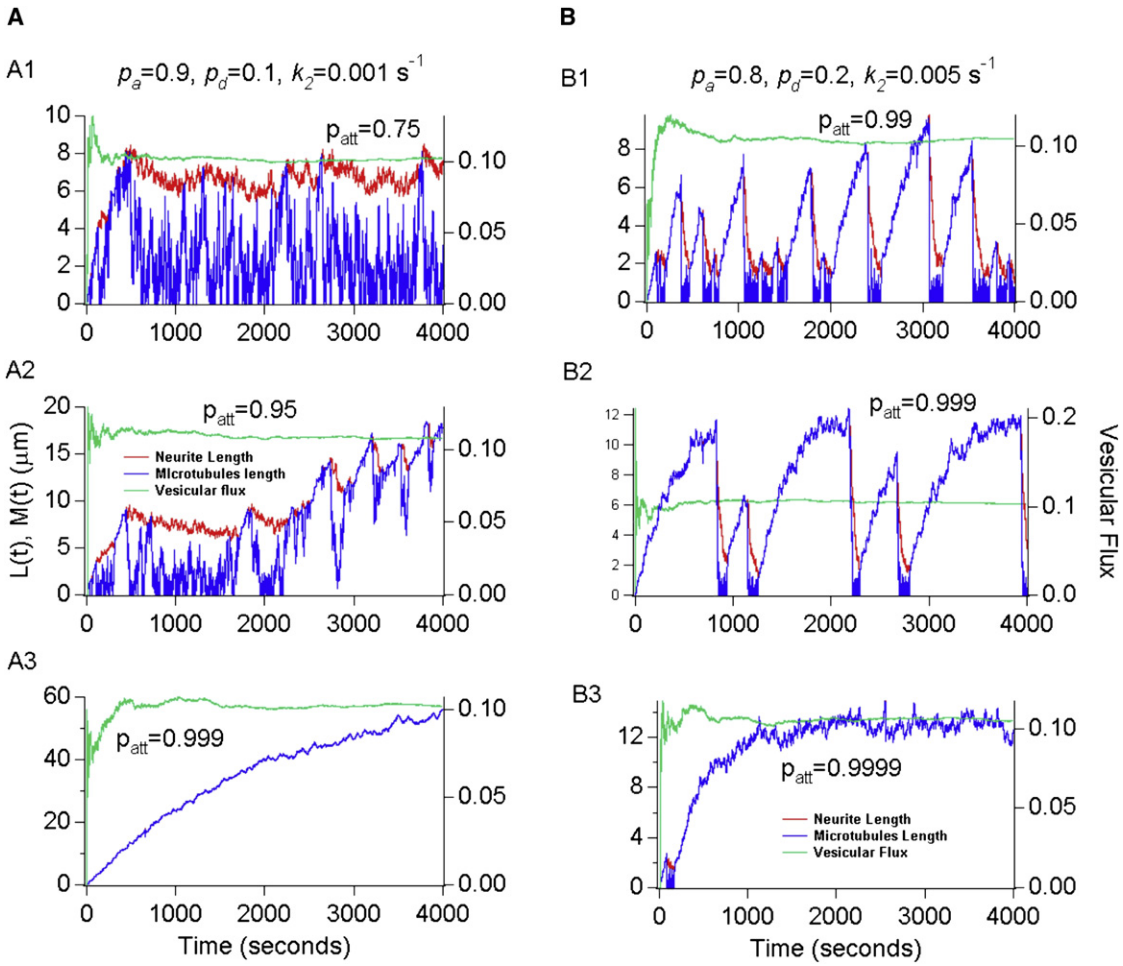

FIGURE 4 Simulated neurite and microtubules lengths using Eqs. 44–48 and $N_0 = 6000$. For a given set of parameters (*A* and *B*) we have increased the attachment probability p_{att} until we obtain stable growth. (*A*) Langevin simulations of the neurite and microtubules lengths for the parameter values given in Table 1 and $p_a = 0.9$, $p_d = 0.1$, and $k_2 = 0.001$ s^{-1} (52,55). (*B*) Langevin simulations of the neurite and microtubules lengths for the parameter values given in Table 1 and $p_a = 0.8$, $p_d = 0.2$, and $k_2 = 0.005$ s^{-1} (52,55). The red traces denote neurite length $L(t)$, blue traces denote microtubules bundle length $M(t)$, and green traces indicate the flux of vesicles at the neurite tip, i.e., vesicles/second. As discussed in the text, the simulations show three main regimes, which represent: collapse (*A*1), oscillation (*A*2, *B*1, and *B*2) corresponding to dendritic growth and stable elongation (*A*3 and *B*3) associated with axonal growth.

*B*2), the overall dynamics shows large oscillations between two equilibrium values, imposed by the two endocytosis rate constants (k_2) determined by whether or not the MT bundle is attached to the actin network at the neurite tip (51,52) (see also Appendix 3). Because the microtubules bundle in Fig. 4, *B*1 and *B*2, is less stable than in Fig. 4 *A*2, periods where it is detached from the neurite are characterized by strong collapse of both structures. In comparison, in Fig. 4 *A*2 because the endocytosis rate constant is lower than in Fig. 4 *B*, a collapse in the microtubules bundle does not lead to neurite collapse. The second regime reflects the dynamical effects of signaling on the microtubules-neurite attachment and endocytotic pathways. Indeed, it has been shown experimentally that in the presence of Ephrin A2 and Semaphorin 3A, the rate of endocytosis is increased (51,52). When neuronal activity dynamically modulates the concentration of these molecules, we predict that the neurite length will be described by the second oscillatory regime.

Finally in a third regime, shown in Fig. 4, *A*3 and *B*3, both the microtubules bundle and the neurite stay attached together and thus the length of the system converges to a steady length determined by the weaker endocytosis rate. Furthermore, the regime shown in Fig. 4 *A*3 fits with axonal outgrowth, since 50 μm in 4000 s corresponds to an average speed of 45 μm/h, in the range of observations for the extension of long neurites, i.e., axons (5).

To explore a growth regime dominated by the vesicular transport, we decrease the vesicular flux from 6000 to 600 available vesicles in the cell body keeping all other parameters fixed as in Fig. 4 and run identical simulations for

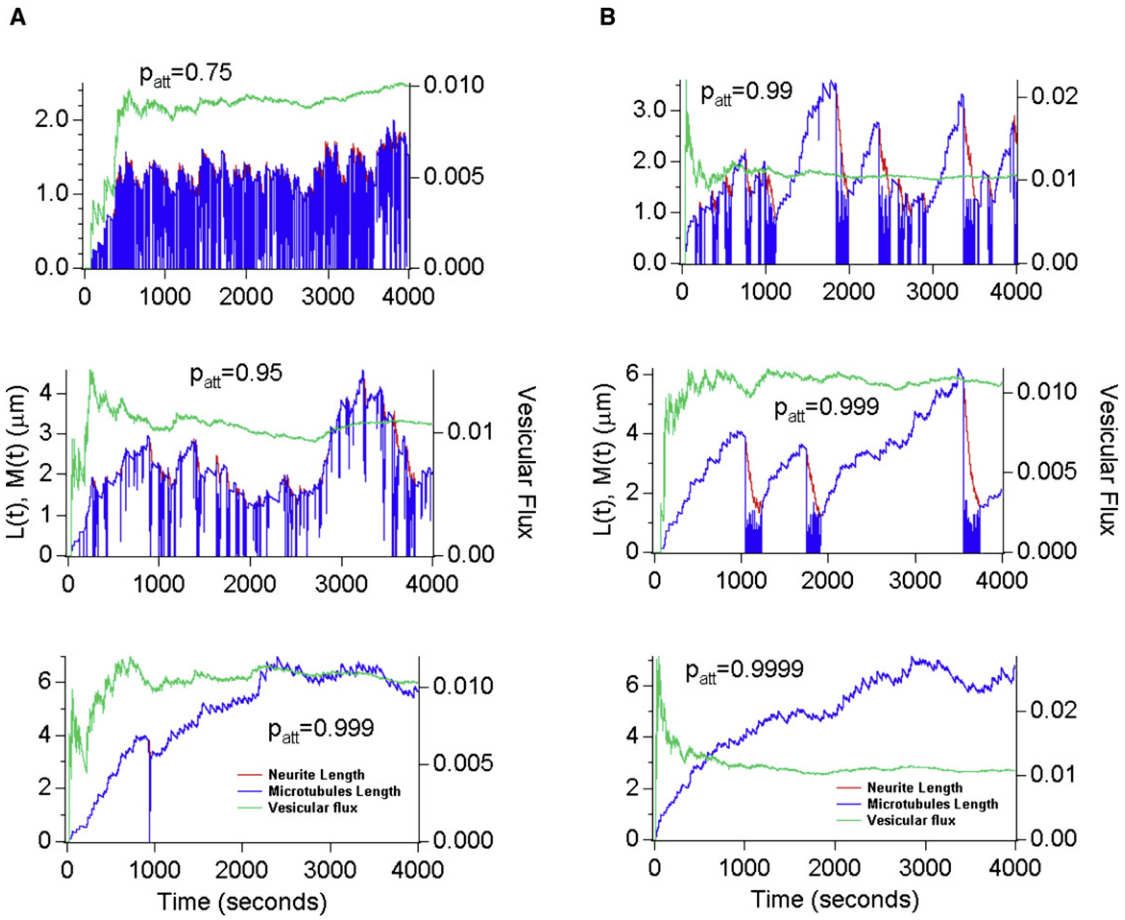

FIGURE 5 Simulated neurite and microtubules lengths using Eqs. 44–48 and $N_0 = 600$. For a given set of parameters (*A* and *B*) we have increased the attachment probability p_{att} until we obtain stable growth. (*A*) Langevin simulations of the neurite and microtubules lengths for the parameter values given in Table 1 and $p_a = 0.9$, $p_d = 0.1$, and $k_2 = 0.001\ s^{-1}$ (52,55). (*B*) Langevin simulations of the neurite and microtubules lengths for the parameter values given in Table 1 and $p_a = 0.8$, $p_d = 0.2$, and $k_2 = 0.005\ s^{-1}$ (52,55). The red traces denote neurite length $L(t)$, blue traces denote microtubules bundle length $M(t)$, and green traces indicate the flux of vesicles at the neurite tip, i.e., vesicles/second.

different values of p_{att}. We find profound effects in the simulation illustrated in Fig. 5. This points out the crucial role of the exocytosis process, even when microtubules (MTs) are stable. These simulations also show that when the vesicles number is a limiting factor, even when the microtubules are very stable, no long neurites can be generated. It is also interesting to note that the dynamical fluctuations (oscillations) we have found, definitely originate in the cytoskeletal dynamics and do not depend on the total amount of vesicles. However, in the absence of vesicles, no dendrites and axons could be formed, regardless of the degree of microtubules stability.

We conclude that depending on the degree of interaction among the microtubules, actin network, and membrane addition, neurite growth occurs in various regimes. These regimes are regulated by two endocytosis rate constants determined by whether or not the MT bundle is attached to the actin network at the neurite tip (51,52) (see also Appendix 3). Therefore, depending on the value of p_{att}, the neurite dynamics can switch between two states.

Estimation of the neurite length using the measured TI-vamp vesicular flux

In the theoretical approach presented in the previous section, we predicted that the secretory vesicle flux determines the neurite growth rate. Now, using experimental data, we confirm that TI-VAMP but not Syb2 flux determines the neurite outgrowth rate. To assess this question, we measure the vesicles motion in the neurite. Fast growing neurites expressing both mRFP-TI-VAMP and EGFP-Syb2 were recorded every minute over a time period of 1–2 h just after the onset of staurosporine treatment (Fig. 6 *A*). As shown in Fig. 6 *B* the onset of fluorescence for mRFP-TI-VAMP occurred earlier than EGFP-Syb2, suggesting that TI-VAMP-mediated exocytosis may be required. To confirm that the neurite growth can be attributed to the fusion of the TI-VAMP vesicles, by using fluorescence intensity (see Fig. 7), we extracted the vesicular flux at the neurite (see *Stage 2* in Fig. 7). Then, using the flux formula given by Eq. 21, we computed the neurite length numerically and compared it with the experimental

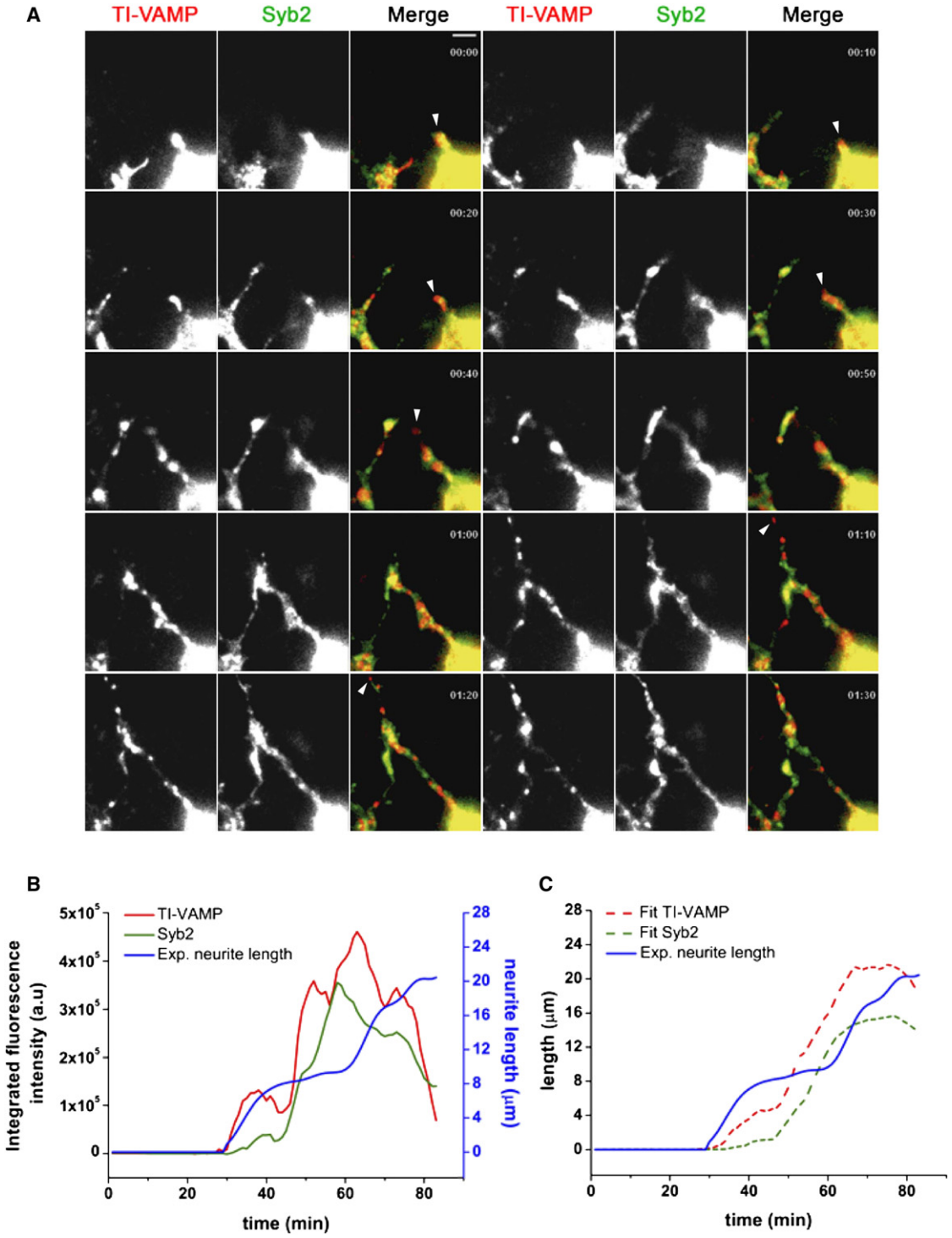

FIGURE 6 TI-VAMP but not Syb2 accounts for neurite extension at early stage. (*A*) PC12 cells were co-transfected with mRFP-TI-VAMP (*red*) and EGFP-Syb2 (*green*). Neurite outgrowth is shown after the onset of neuritogenesis (00:00, h/min) induced by treatment with 100 nM staurosporine and followed by online video imaging over a time period of 1 h and 30 min (see Movie S1 and Movie S2 in Supporting Material). Note that TI-VAMP vesicles often accumulated at the tip of the growing neurite (*Arrowheads*. Bar = 5 μm). (*B*) Dynamics of FP-tagged proteins were followed during neurite initiation. Neurite was ideally segmented in seven different stages, from which integrated fluorescence intensity was collected (Fig. 7). The dynamics of fluorescence for mRFP-TI-VAMP (*red continuous line*) and EGFP-Syb2 (*green continuous line*) from one single stage and the length of neurite over the time were shown in the graph. (*C*) We generated neurite length using Eq. 21 from the experimentally measured fluorescence for the two types of vesicles, TI-VAMP (*red dashed line*) and Syb2 (*green dashed line*), and compared them with the experimental neurite length. The "Fitted TI-VAMP" curve fits the experimental neurite length curve better than "Fitted Syb2."

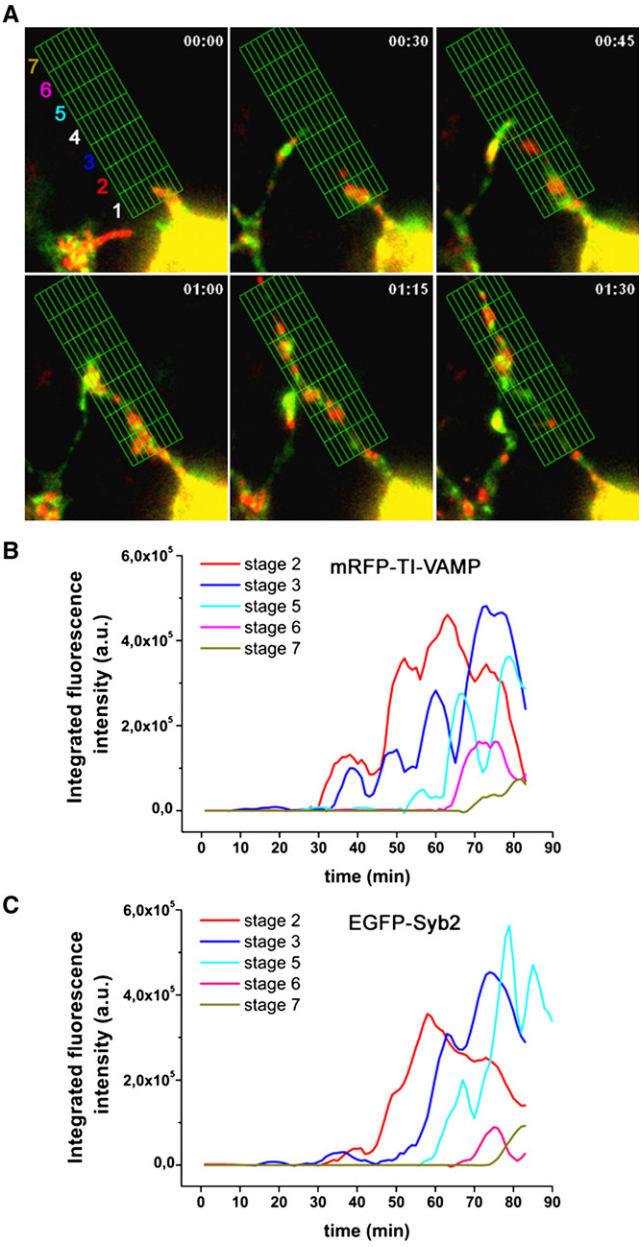

FIGURE 7 Quantification of fluorescence intensity during neurite outgrowth. (*A*) Selected frames from Movie S2 show the mRFP-TI-VAMP (*red*) and EGFP-Syb2 (*green*) distribution along the growing neurite. To quantify the dynamics of the two FP-tagged proteins, the selected neurite was ideally segmented in seven stages (*colored numbers*), from the cell body limit to the maximal extent of the process. Then the integrated fluorescent intensity was automatically collected by using the grid module (*green grid*) of Metamorph software and converted in numerical data. The same grid was applied to analyze the dynamics of both FP-tagged proteins in the same selected neurite. Data collected were used to generate curves for every stage allowing comparing the dynamics between mRFP-TI-VAMP (*B*) and EGFP-Syb2 (*C*). In this example, because of movement of soma during the experiment and temporary overlap with a second growing neurite, respectively, neither stage 1 nor stage 4 were considered for the analysis. Only experimental data from stage 1 or 2 were used f or generate neurite length using Eq. 21.

one: to generate the best fit, we calibrated both the flux intensity to match the final length and the endocytosis rate k_2 to recover the dynamics (Fig. 6 *C*). From an optimal fit, we found that $k_2 = 0.075\ \text{min}^{-1}$ ($0.00125\ \text{s}^{-1}$) in good agreement not only with the experimental constant previously published (52,55) but also within the range of values we used in the simulations in Figs. 2, 4, and 5. Furthermore, we observe that only TI-VAMP, but not Syb2 flux, lead to a simulated length compatible with the experimental one (Fig. 6 *C*, Appendix 4). Finally, we checked that the total flux due to the sum of mRFP-TI-VAMP and EGFP-Syb2 could not account for the experimentally measured length, as shown in Fig. 8

Using the fluorescence intensity, we computed the flux of membrane vesicles and compared it to the theoretical estimate. Moreover, the parameter values obtained from our analysis (i.e., the endocytosis rate k_2) agree very well with previously published studies (52,55). Thus, our assumption that the fluorescence intensity is proportional to the number of vesicle appears to be fairly reasonable. Based on our analysis, we conclude that membrane addition during neurite growth is mediated by TI-VAMP but not Syb2 vesicles transport, in agreement with our RNAi experiments.

DISCUSSION

In this study, we have presented a biophysical model of neurite initiation and growth based on complex interactions between secretory vesicles, which deliver membrane to the neurite; microtubules, which stabilize the neurite and guide the vesicles movement; and finally, the neurite itself. Whereas previous theoretical models only considered cytoskeletal components (11–22), in our approach, we describe the neurite dynamics based on microtubule transport and

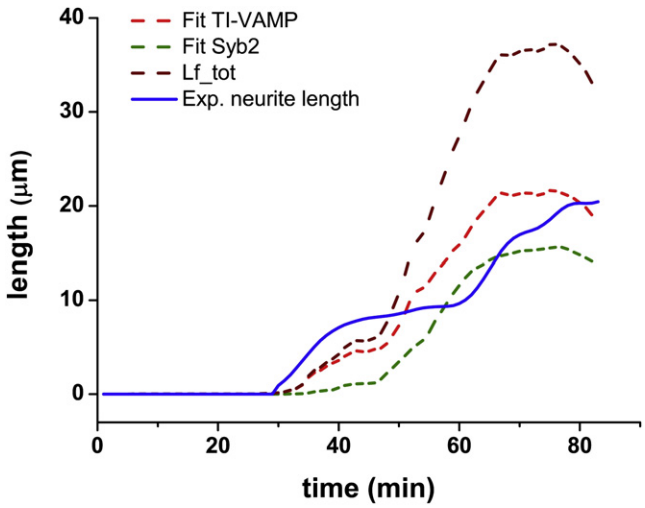

FIGURE 8 Neurite length was generated using Eq. 21 from the experimentally measured fluorescence for the two types of vesicles—TI-VAMP and Syb2—and compared them with the experimental neurite length.

exocytosis and endocytosis rates of secretory vesicles mediating neurite growth. Our approach reveals that the neurite growth is determined by the interaction between microtubule and TI-VAMP vesicular flux measured at the neurite site.

Vesicular flux dynamics at neurite initiation site

Equation 15 provides a quantitative estimate for the flux of vesicles at the neurite initiation site, which we defined as a preferential fusion patch at the plasma membrane for exocytosis. This patch can be better defined by cell autonomous mechanisms such as local concentration of the exocyst complex (31,56,57). Interestingly, the neurite growth can be modulated and, for example, primordial exocytosis at the neurite site could trigger a local activation of Cdc42, which regulates the TI-VAMP vesicles fusion with the plasma membrane.

At this neurite-preferential patch of the plasma membrane, exocytosis or endocytosis would respectively be stimulated (or inhibited), or both, leading to the genesis of a primordial protrusion. Nevertheless, our vesicle-only model shows that neurites of limited lengths are generated, but this result cannot account for the diversity of neurite lengths (axons versus dendrites). In addition, it has been proposed recently that centrosomes, the Golgi apparatus, and endosomes cluster together close to the area where the first neurite is formed, allowing for the generation of axons (38). Further studies should account for the formation of these intermediate structures and explore their specific contribution to the neurite growth process.

The patch of plasma membrane corresponding to the initiation site of neurite growth can also be regulated by environmental cues (58,59): External activity can affect the endocytosis rate k_2; for example, Ephrin A2 expressed in gradient in the tectum produces growth-cone collapse by increasing the F-actin depolymerization and the endocytosis rates (51,52). However, in our experiments of neurite growth using PC12 cells treated with staurosporine, external cues are not required—which is also the case for other cells, including hippocampal neurons in primary culture (60). We thus leave open the prediction of Eq. 37, where this analytical expression generalizes the analysis of Eq. 15, in which a vesicle can now fuse at the neurite tip when it is permitted by external cues activity.

Role of TI-VAMP vesicle versus Syb2 modulation of the vesicular flux

It is interesting that at early stage Syb2 vesicles are secreted, in the absence of formed synapse, and their role is questionable (61). We have indeed confirmed here that they do not contribute directly to membrane expansion. Further, they do not replace TI-VAMP vesicles when their secretion is suppressed. Thus we leave open the question of the role of Syb2 vesicles at this early stage, in good agreement with the lack of effect of the knockout on brain formation (10). In addition, we found that the combined silencing of both Syb2 and TI-VAMP lead to a neurite growth similar to silencing TI-VAMP alone (our unpublished observation). The origin of this primary membrane delivery comes either from a residual TI-VAMP expression or from another source, which would require a detailed investigation.

Vesicular delivery combined with microtubule dynamics determines neurite growth regimes

One of our findings is that based on vesicular delivery only, the neurite dynamics is very limited and cannot change at different rates. In contrast, when we include in our model the microtubule dynamics and incorporate the neurite-microtubules interaction parameter p_{att}, we find various modes of neurite growth. However, for a limited vesicular flux (Fig. 5), our simulations show that longer neurites cannot form. We attribute this phenomenon to a drastic limitation of membrane supply. Taken altogether, these results indicate that vesicles are necessary but not sufficient for the extension of longer neurites (dendrites and axons).

As discussed in the previous section, the parameter p_{att} measures the probability that the microtubules bundle stays attached to the neurite tip. Anchored together, both structures are stabilized. The probability p_{att} accounts for various molecular phenomena including the microtubules-actin interaction, and the dynamics of microtubules tips and actin microfilaments. Random and disorganized microtubule dynamics have been reported to be responsible for the large dendritic growth fluctuations (35). This case is obtained in our simulation (Fig. 4) for a low probability value of the attachment parameter p_{att}. In that case, the neurite is characterized by periods where the neurite and the microtubules are detached. Thus both structures can oscillate between their own independent behavior and a correlated one, when they are attached together. In contrast, the well-organized axonal microtubules (35) are associated with a high value of p_{att}, preventing both structures to be independent.

We account for the coupling between the microtubules and the neurite by decreasing the endocytosis rate in the entire neurite. In fact there are experimental evidences for such global stabilization during formation and elongation of axons (62). We consider here that the interactions between the microtubules and the neurite stabilize both structures by generating a higher potential barrier for endocytosis, not only at the point of contact but everywhere. This view assumes that the tension generated by a bundle of organized microtubules can be felt by the entire neurite. An experimental verification of this phenomenon would be interesting.

We conclude that the catastrophe (Fig. 4 *A*1) and oscillation (Fig. 4, *B*1 and *B*2) regimes correspond to the dendritic growing mode, while the stable growth regime (Fig. 4, *A*3 and *B*3) may reflect the axon growth. In the case of more stable microtubules (Fig. 4 *A*3) we find less dynamical fluctuation and increasing growth, which can explain the higher

axon elongation compared to neurite. This finding agrees with the experimental observation reported in tubulin-tyrosin-ligase mutant mice (63) as well as in Witte et al. (64), who show that microtubules in the axon are more stable than those in other neurites. Because the neurite stabilization depends on the interaction between the microtubules and the actin network, we predict that affecting the actin network should result in an increase of the neurite dynamics, switching from axonal to dendritic growth mode. Possibly, the fusion of vesicles at the neurite tip is actin-dependent as demonstrated in the case of TI-VAMP (23) and thus by disrupting actin, the overall growth will be slower.

Parameter values

Since our model is based on physical properties of the cell, it should, in principle, apply to a wide range of biological systems where protrusions are formed in such a manner. We have indeed applied this approach to neuronal genesis and thus chosen parameter values within the range measured in experimental studies of neuronal cultures or PC12 cells. In the case of microtubules assembly/disassembly rates, however, such data is limited; therefore, we have taken these rates from in vitro studies with purified tubulin (12).

In our model, all vesicles contributing to the membrane delivery are initiated at the cell body and we neglected, in first approximation, local vesicle synthesis and trafficking generated in the dendrites. In our microscopic description, we have neglected active retrograde motion of vesicles, but not retrograde motion due to diffusion. In addition, an endocytosed vesicle contributes to decreasing the neurite length, but does not contribute to the fluorescence intensity, since only vesicles generated at the cell soma have been labeled with fluorescent tags. The drift amplitude that we are using is thus the difference between the forward minus the backward drift.

CONCLUSION

We have shown here that neurite initiation and growth are based on complex interactions between vesicles, to deliver membrane to the neurite; microtubules, to stabilize the neurite and guide the vesicles movement; and the actin network that controls the degree of interaction between the microtubules and the neurite. We conclude from our model that vesicular transport on the microtubule network, from the cell body to the periphery of undifferentiated neuronal cells, allows for microtubules and diffusion to guide vesicles to the nascent neurite in the sense that finding the neurite site relies now on a two-dimensional diffusion/sequestration at the cell surface, which is quite fast compared to a three-dimensional search. Neurite elongation is characterized by complex neurite-microtubules interactions. These neurite-microtubule interactions are critical to promote long protrusion extension and the parameter that regulates these interactions may thus be a fundamental feature of neuronal cell development. Our model can also be used to explain and predict the growth of other cellular processes including pollen tube (65,66) and fungi hyphal tip growths (8,67) that depend on the same basic mechanisms and respond to similar biological constraints. It would be interesting to extend our model to study neuronal growth modulated by activity and also how microtubule and vesicular delivery reorganize during neuronal regeneration and repair.

APPENDIX 1: CALIBRATION PROCEDURE FOR AN EFFECTIVE DRIFT

The calibration procedure consists in estimating the steady-state potential drift ϕ from a steady situation where no neurites can grow. We look for the steady-state distribution of vesicles inside a cellular domain that contains a bundle of microtubules. The method consists of generating a Brownian simulation of many vesicles inside the cell that are all reflected at the boundary. We consider the solution of the Fokker-Planck equation (FPE) associated with Eq. 3. In this procedure, we restrict the analysis to a repulsive drift that points toward the cell boundary. For a spherical cell, we approximate the potential as radially symmetric, given by

$$\phi(\boldsymbol{x}) = \alpha|\boldsymbol{x}|, \tag{23}$$

where α is a constant to be determined. The Brownian simulations are represented in Fig. 1. To derive the fitting curve, we recall that the steady-state distribution of independent vesicles is obtained by solving the Fokker-Planck equation. The pdf $p_v(\boldsymbol{x},t)$ of finding a stochastic vesicle at location $\boldsymbol{x}$ at time t is given by Schuss (43) as

$$p_v(\boldsymbol{x},t|\boldsymbol{x}_0)d\boldsymbol{x} = Pr\{\boldsymbol{x}(t)\in\boldsymbol{x} + d\boldsymbol{x}|\boldsymbol{x}(0) = \boldsymbol{x}_0\}. \tag{24}$$

It satisfies the forward equation

$$\frac{\partial p_v}{\partial t} = D\Delta p_v - \nabla(\nabla\phi \cdot p_v) \tag{25}$$

when the boundary probability flux

$$\mathbf{J}.\mathbf{n} = -D\frac{\partial p_v}{\partial n} + p_v\frac{\partial \phi}{\partial n} \tag{26}$$

vanishes at the cell boundary; that is, when all vesicles are reflected and thus cannot fuse with the cell membrane, the steady-state solution of Eq. 5 is given by

$$p_v(\boldsymbol{x}) = Ce^{\phi(\boldsymbol{x})/D}, \tag{27}$$

where C is constant which is determined by the normalization condition

$$\int_{\Omega} p_v(\boldsymbol{x})d\boldsymbol{x} = 1. \tag{28}$$

For N_0 independent vesicles, the steady distribution p_{st} is given as

$$p_{st}(\boldsymbol{x}) = N_0 p_v(\boldsymbol{x}). \tag{29}$$

For a constant drift velocity $(\partial\phi/\partial r) = \vartheta$ in radial direction, Eq. 27 becomes

$$p_v(r) = Ce^{\frac{\vartheta}{D}r} \quad \text{for} \quad 0 < r \leq R. \tag{30}$$

The steady-state distribution p_{st} is given by

$$p_{\mathrm{st}}(r) = \frac{\vartheta}{2\pi D\left(Re^{\frac{\vartheta R}{D}} - \frac{D}{\vartheta}e^{\frac{\vartheta R}{D}} - 1\right)}e^{\frac{\vartheta r}{D}} \quad (31)$$

$$\text{for } 0 < r \leq R \text{ in dimension 2,}$$

$$= \frac{\vartheta}{4\pi D\left(R^2 e^{\frac{\vartheta R}{D}} - \frac{D}{\vartheta}\left(Re^{\frac{\vartheta R}{D}} - \frac{D}{\vartheta}\left(e^{\frac{\vartheta R}{D}} - 1\right)\right)\right)}e^{\frac{\vartheta r}{D}} \quad (32)$$

$$\text{for } 0 < r \leq R \text{ in dimension3.}$$

We chose ϑ such that the distribution of vesicles generated by simulations of the stochastic Eq. 3 fits the histogram generated by the empirical process Eq. 2 in dimension 2.

APPENDIX 2: NEURITE GROWING RATE MODULATED BY INTERMITTENT NEURONAL ACTIVITY AND NEURITE GROWTH

To include the effect of the environmental activity on the neurite growth, we propose to extend Eq. 15. Such environmental activity may represent the mean number of cues released by the neighboring neurons. Indeed, it has been reported experimentally that neurotrophins (27,58,59), can play a key role in regulating neurite growth. To account for this mechanism, we incorporate this effect by defining a fusion rate that depends both on the dynamics of external cues and vesicles arrival. Thus, in this scenario, vesicles fusion is controlled by presence of external cues at the site where vesicles fuse. Our computations assume that cues arrive at random times, distributed uniformly during a periodic interval of time of length T. We assume that during a fraction of time T_{a}, through unknown signaling process, cues allow vesicles to fuse. The fusing time T_{a} is chosen uniformly distributed during each period T with a density probability function given by $p(u) = 1/T\chi_{[0,T]}$, where χ is a step function. Thus the mean vesicles fusing time T^* is given by

$$T^* = \int_0^T up(u)du = \frac{1}{T}\int_0^T udu = \frac{T}{2}. \quad (33)$$

To compute the rate of vesicles fusion, we consider the joint event that a vesicle arrives and some cues are located on the neurite tip. Thus the mean time a vesicle is allowed to fuse can be decomposed into an infinite sum of mean times a vesicle fuses in the k^{th} time interval, which receives cues during a time u_{k} (distributed according to p),

$$\tau_{\mathrm{k}}(u_{\mathrm{k}}) = \int_0^\infty t\frac{d}{dt}Pr\left\{\tau^{\mathrm{arrive}} < t, kT < \tau^{\mathrm{arrive}} < kT + u_{\mathrm{k}}\right\}dt,\ k = 0, 1, 2, \ldots. \quad (34)$$

The total mean time is defined by

$$E\tau = \sum_{\mathrm{k}=0}^{\infty}\left\langle E\tau_{\mathrm{k}}(u_{\mathrm{k}})\right\rangle = \sum_{\mathrm{k}=0}^{\infty}\int_0^T\int_0^\infty t\tfrac{d}{dt}\Pr\{\tau^{\mathrm{arrive}} < t, kT < \tau^{\mathrm{arrive}} < kT + u_{\mathrm{k}}\}dtp(u_{\mathrm{k}})du_{\mathrm{k}}. \quad (35)$$

Since the arrival time of the vesicles to the small hole is Poissonian (42),

$$\Pr\{kT < \tau^{\mathrm{arrive}} < kT + u_{\mathrm{k}}\} = \int_{kT}^{kT+u_{\mathrm{k}}} \lambda e^{-\lambda x}dx$$

$$\Pr\{\tau^{\mathrm{arrive}} < t\} = 1 - e^{-\lambda t},$$

where $\lambda = 1/\overline{\tau}_\delta = \kappa_\delta$, we get

$$E\tau = \int_0^\infty t\lambda e^{-\lambda t}dt\sum_{\mathrm{k}=0}^{\infty}\int_0^T\int_{kT}^{kT+u_{\mathrm{k}}}\lambda e^{-\lambda x}dx\frac{1}{T}\chi_{[0,T]}du_{\mathrm{k}}. \quad (36)$$

Consequently

$$E\tau = \frac{1}{\lambda}\frac{1}{T}\sum_{\mathrm{k}=0}^{\infty}\left(\int_0^T\left(-e^{-\lambda kT + u_{\mathrm{k}}} + e^{-\lambda kT}\right)\chi_{[0,T]}du_{\mathrm{k}}\right),$$

$$E\tau = \frac{1}{\lambda}\frac{1}{T}\sum_{\mathrm{k}=0}^{\infty}e^{-\lambda kT}\left(\int_0^T\left(1 - e^{-\lambda u_{\mathrm{k}}}\right)\chi_{[0,T]}du_{\mathrm{k}}\right).$$

Thus, we obtain the final formula

$$\overline{\tau} = E\tau = \frac{1}{\lambda}\frac{1}{T}\left(\frac{1}{1 - e^{-\lambda T}}\right)\left(T - \frac{1 - e^{-\lambda T}}{\lambda}\right). \quad (37)$$

APPENDIX 3: VESICLES AND MICROTUBULES DYNAMICS IN THE GROWING NEURITE

To further investigate how neurite extends and elongates, we add the effect of microtubules to the previous model. Microtubules can interact with neurite growth by first directing vesicles inside the neurite and second by attaching to the neurite tip. When the microtubules bundle is attached to the neurite, both are stabilized (33,34,51,52). We study here the properties of the overall system, which consists in trafficking vesicles and a unique microtubules bundle interacting with the growing neurite. The analysis starts when vesicles are delivered at the proximal (near to the cell body) end of the neurite (31,37,40). We continue to approximate the neurite geometry as a long and thin cylinder, where a schematic diagram of the model is presented in Fig. 3. We model the neurite tip as a narrow layer of length ε, which implicitly accounts for the submembrane F-actin bundles that can stabilize the microtubules attached to it (33,34). We consider the vesicular motion as one-dimensional. In our model the growing neurite of length $L(t)$ interacts with the microtubules bundle of length $M(t)$ and the vesicle dynamics. We denote by $J(x, t)|_{x=L(t)}$ the flux of vesicles at the tip of the neurite.

In our description, vesicles are injected at the base of the neurite with a Poissonian rate κ_δ given by Eq. 4 and are removed when they arrive at the tip of the neurite. The equation of vesicles motion in the dendrite in a homogenized version is given by Eq. 2 can be written as

$$\dot{\mathbf{X}} = \boldsymbol{\vartheta}_0 + \sqrt{2D}\dot{\boldsymbol{\omega}}, \quad (38)$$

where $\boldsymbol{\vartheta_0}$ is the drift directed toward the neurite tip, and D is the effective diffusion constant in the cytoplasm. Vesicles move inside the neurite until they reach the distal neurite tip, where exocytosis occurs with a certain probability (27,31,32,40,53). At the neurite tip, each fusing vesicle contributes l_0 length to the total membrane surface of the neurite. Equation 38 is a homogenization approximation of the real movement, which ignores that the microtubules can occupy only a small fraction of the neurite, while the vesicles movement is purely random. For N independent vesicles, we define the density of vesicles per unit length N_{v}, which is a solution of

$$\frac{\partial N_{\mathrm{v}}}{\partial t} = D\frac{\partial^2 N_{\mathrm{v}}}{\partial x^2} - \vartheta_0\frac{\partial N_{\mathrm{v}}}{\partial x}. \quad (39)$$

The flux of vesicle at position x is

$$J(x,t)|_{x} = -\left(D\frac{\partial N_v(x,t)}{\partial x} - \vartheta_0 N_v(x,t)\right). \quad (40)$$

N_v satisfies the boundary conditions

$$N_v(L(t),t) = 0 \text{ for total absorption}, \quad (41)$$

and

$$J(0,t)|_{x=0} = N_0\kappa_\delta. \quad (42)$$

Equation 41 can also be replaced by a partial absorption condition

$$J(x,t)|_{x=L(t)} = -k_{ab}N_v|_{x=L(t)}, \quad (43)$$

where N_0 is the number of vesicles inside the soma and k_{ab} is a constant of absorption. The partial absorbing boundary condition means that either a vesicle fuses with a certain probability or when it fuses only a certain fraction of the surface membrane is added to the neurite surface.

Modeling the second phase of neurite growth: vesicle-microtubule-neurite interplay

The second phase starts when vesicles arrive at the neurite base, which is modeled as a Poisson process. Thus vesicles are injected at the soma/neurite interface at a rate κ_δ given by Eq. 15 and the number of injected vesicles N_i is given by

$$N_i(t+\Delta t) = \begin{cases} N_i(t)+1, & \text{with probability } \kappa_\delta\Delta t \\ N_i(t), & \text{with probability } 1-\kappa_\delta\Delta t \end{cases}. \quad (44)$$

Once inside the neurite, vesicles motion is described by Eq. 38, until fusion at the neurite tip occurs (53). Meanwhile the microtubules bundle length M grows according to the rule

$$M(t+\Delta t) = M(t) + \begin{cases} k_a\Delta t, & \text{with probability } p_a\Delta t \\ -k_d\Delta t, & \text{with probability } p_d\Delta t \\ 0, & \text{with probability } 1-(p_a+p_d)\Delta t \end{cases}, \quad (45)$$

where p_a (or k_a) is the microtubules probability (or rate) to grow (assemble of tubulin dimers (12,34,54,68,69)) and p_d (or k_d) is the probability (or rate) to shrink (disassemble). We also include a probability $1-p_a\Delta t-p_d\Delta t$ that microtubules length M does not change during time Δt. When the microtubules end reaches the neurite tip, they can interact and attach with a probability p_{att}, which accounts for the experimental observations reported in the literature (33,34). When attached to the neurite tip, microtubules dynamics changes as suggested experimentally (54) and neurites undergo persistent growth governed by vesicles exocytosis. Thus, in our model, when microtubules are attached to the neurite tip, the rate of change of the microtubules length is the same as the rate of change of the neurite length. Finally, the microtubules bundle length interacting with a neurite is modeled as

$$M(t+\Delta t) = \begin{cases} L(t+\Delta t), & \text{if } M(t) > L(t)-\grave{o} \\ & \text{with probability } p_{att}\Delta t \\ M(t+\Delta t), & \text{if } M(t)\le L(t)-\grave{o} \end{cases}. \quad (46)$$

When the microtubules bundle reaches the neurite tip, both are stabilized and this coupling affects the endocytosis rate $k_2(M)$, given by

$$k_2(M) = \begin{cases} \sigma_v' k_2, & \text{if } M(t) > L(t)-\grave{o} \;\&\; p_{att}\Delta t \\ \sigma_v'' k_2, & \text{if } M(t)\le L(t)-\grave{o} \;\&\; \text{otherwise} \end{cases}. \quad (47)$$

The parameters σ'_v and σ''_v measure the membrane vesicles endocytosis with and in the absence of the microtubules bundle attached to the neurite. The decay of the endocytosis rate (51,52) when the bundle is attached corresponds to a stabilization mechanism (33,34) and is based on the idea that an attached bundle increases the minimal surface tension necessary to form a vesicle by endocytosis.

Finally the neurite length increases proportionally to the flux of vesicles fusing at the tip of the neurite and decay due to vesicles endocytosis, thus the dynamics is

$$L(t+\Delta t) = L(t) + \left(l_0 J(x,t)|_{x=L(t)} - k_2(M)L(t)\right)\Delta t. \quad (48)$$

Rough steady-state analysis

We now present a rough steady-state analysis of the growing neurite interacting with the microtubule dynamics. We model the coupling between the microtubules and the neurite, in part in the endocytosis decay rate, which increases during neurite retraction (51,52). As shown experimentally in the literature (33,34), when a microtubule reaches the neurite tip, it may attach and stabilize the growing structure. This is taken into account by changing the neurite decay rate $k_2(M)$ in our simulations. Hence we have the following rule:

$$k_2(M,t) = \begin{cases} k_2^a, & \text{when the microtubule is attached} \\ k_2^d, & \text{when the microtubule is free} \end{cases}, \quad (49)$$

where $k^a{}_2 < k^d{}_2$. Thus, the neurite mean length dynamics is given by

$$\frac{dL}{dt} = l_0 J(x,t)|_{x=L(t)} - k_2(M,t)L, \quad (50)$$

where l_0 is the step increment of length after a single vesicle fuses with the neurite membrane. When the neurite and the dendrite are all the time attached together, $k_2(M,t) = k^a{}_2$ and then the steady-state analysis gives that the solution of Eq. 39 together with the boundary conditions (from Eqs. 41 and 42) is given by

$$N_v(x) = \frac{N_0\kappa_\delta}{\vartheta_0}\left(1 - e^{-\frac{\vartheta_0}{D}L}e^{\frac{\vartheta_0}{D}x}\right), \quad \text{for} \quad 0\le x\le L, \quad (51)$$

while with the boundary conditions shown in Eqs. 42 and 43, it is given by

$$N_v(x) = \frac{N_0\kappa_\delta}{\vartheta_0}\left(1 - \frac{\vartheta_0 + k_{ab}}{k_{ab}}e^{-\frac{\vartheta_0}{D}L}e^{\frac{\vartheta_0}{D}x}\right), \quad \text{for} \quad 0\le x\le L. \quad (52)$$

Finally, the steady-state solution of Eq. 50 is

$$L_{st.st.} = \frac{l_0 J(x,t)|_{x=L(t)}}{k_2^a}, \quad (53)$$

and after substitution of Eqs. 51 and 52, we obtain that

$$L_{st.st.} = \frac{l_0 N_0 \kappa_\delta}{k_2^a}. \quad (54)$$

APPENDIX 4: STATISTICAL ANALYSIS

One-way ANOVA report: comparing experimentally measured length and the fit from Syb2 fluorescence

See Table 2 below.

TABLE 2 Basic samples statistics

Treatment	Name	Samples	Sum	Mean	Variance
0	L_{exp}	89	729.8	8.2	58.15
1	L_{Syb2}	89	495.5	5.568	40.3

Homogeneity of variance

Levene's test $F = 1.757$, $P = 0.1867$.

Levene's test indicates homogeneous variance at >1% significance level. See Table 3 below.

TABLE 3 Analysis of variance

Analysis of variance	DF	Sum squares	Mean square	F	Probability
Between treatments	1	308.3	308.3	6.263	0.0132
Within treatments	176	8664	49.22		
Total	177	8972	357.5		

Total samples = 178; sample mean = 6.884; variance of sample mean = 1.732; and treatment component of variance = 2.911.
DF, distribution function; F, the value of the F statistic that measures the variation in the means of the treatments.

Pairwise treatment differences

See Table 4 below.

TABLE 4 Pairwise treatment tests

Treatments	Difference of means	Standard error	Span	SRT	Probability
Tukey HSD test					
0, 1	2.632	1.052	2	3.539	0.01325*
Newman Keuls test					
1, 0	2.632	1.052	2	3.539	0.01325*
Dunnett's test (control is treatment 0)					
1, 0	2.632	1.052	$t = 2.503$		0.01324**

SRT, Studentized Range statistic.
*Significant at 5% level.
**Significant at 1% level.

One-way ANOVA report: comparing experimentally measured length and the fit from TI-VAMP fluorescence

See Table 5 below.

TABLE 5 Basic samples statistics

Treatment	Name	Samples	Sum	Mean	Variance
0	L_{exp}	89	729.8	8.2	58.15
1	$L_{TI-VAMP}$	89	745.7	8.378	72.58

Homogeneity of variance

Levene's test $F = 2.397$, $P = 0.1233$.

Levene's test indicates homogeneous variance at >/1% significance level.

See Table 6 below.

TABLE 6 Analysis of variance

Analysis of variance	DF	Sum squares	Mean square	F	Probability
Between treatments	1	1.42	1.42	0.02173	0.883
Within treatments	176	1.15e + 04	65.36		
Total	177	1.15e + 04	66.78		

Total samples = 178; sample mean = 8.289; variance of sample mean = 0.00798; and treatment component of variance = −0.7184.
DF, distribution function; F,the value of the F statistic that measures the variation in the means of the treatments.

Pairwise treatment differences

See Table 7 below.

TABLE 7 Pairwise treatment tests

Treatments	Difference of means	Standard error	Span	SRT	Probability
Tukey HSD test					
0, 1	0.1787	1.212	2	0.2085	0.883*
Newman Keuls test					
0, 1	0.1787	1.212	2	0.2085	0.883*
Dunnett's test (control is treatment 0)					
1, 0	0.1787	1.212	$t = 0.1474$		0.883**

SRT, Studentized Range statistic.
*Significant at 5% level.
**Significant at 1% level.

SUPPORTING MATERIAL

Two movies are available at http://www.biophysj.org/biophysj/supplemental/S0006-3495(08)00110-0.

We are grateful to Nathalie Rouach and Pietro De Camilli for critical reading of the manuscript.

D.H. was partially supported by an European Research Council starting grant and a Neuro-Informatics grant. T.G. was also supported in part by grants from the Institute National de la Santé et de la Recherche Médicale (Avenir Program), the Ville de Paris, Association Française Contre les Myopathies, and Fondation pour la Recherche Médicale. A.B. was supported by fellowships from The French Institute of Health and Medical Research (INSERM) and Association Française Contre les Myopathies.

REFERENCES

1. da Silva, J. S., and C. G. Dotti. 2002. Breaking the neuronal sphere: regulation of the actin cytoskeleton in neuritogenesis. *Nat. Rev. Neurosci.* 3:694–704.
2. Burnette, D. T., A. W. Schaefer, L. Ji, G. Danuser, and P. Forscher. 2007. Filopodial actin bundles are not necessary for microtubule advance into the peripheral domain of Aplysia neuronal growth cones. *Nat. Cell Biol.* 9:1360–1369.
3. Bouquet, C., M. Ravaille-Veron, F. Propst, and F. Nothias. 2007. MAP1B coordinates microtubule and actin filament remodeling in adult mouse Schwann cell tips and DRG neuron growth cones. *Mol. Cell. Neurosci.* 36:235–247.
4. Dent, E. W., and F. B. Gertler. 2003. Cytoskeletal dynamics and transport in growth cone motility and axon guidance. *Neuron.* 40:209–227.
5. Futerman, A., and G. Banker. 1996. The economics of neurite outgrowth–the addition of new membrane to growing axons. *Trends Neurosci.* 19:144–149.
6. Dequidt, C., L. Danglot, P. Alberts, T. Galli, D. Choquet, et al. 2007. Fast turnover of L1 adhesions in neuronal growth cones involving

both surface diffusion and exo/endocytosis of L1 molecules. *Mol. Biol. Cell.* 18:3131–3143.

7. Kamiguchi, H., and F. Yoshihara. 2001. The role of endocytic L1 trafficking in polarized adhesion and migration of nerve growth cones. *J. Neurosci.* 21:9194–9203.
8. Taheri-Talesh, N., T. Horio, L. Araujo-Bazan, X. Dou, E. A. Espeso, et al. 2008. The tip growth apparatus of *Aspergillus nidulans*. *Mol. Biol. Cell.* 19:1439–1449.
9. Osen-Sand, A., J. K. Staple, E. Naldi, G. Schiavo, O. Rossetto, et al. 1996. Common and distinct fusion proteins in axonal growth and transmitter release. *J. Comp. Neurol.* 367:222–234.
10. Schoch, S., F. Deak, A. Konigstorfer, M. Mozhayeva, Y. Sara, et al. 2001. SNARE function analyzed in synaptobrevin/VAMP knockout mice. *Science.* 294:1117–1122.
11. Edelstein-Keshet, L., and G. B. Ermentrout. 2000. Models for spatial polymerization dynamics of rod-like polymers. *J. Math. Biol.* 40:64–96.
12. Fygenson, D. K., E. Braun, and A. Libchaber. 1994. Phase diagram of microtubules. *Phys. Rev. E Stat. Phys. Plasmas Fluids Relat. Interdiscip. Topics.* 50:1579–1588.
13. Margolin, G., I. V. Gregoretti, H. V. Goodson, and M. S. Alber. 2006. Analysis of a mesoscopic stochastic model of microtubule dynamic instability. *Phys. Rev. E. Stat. Nonlin. Soft Matter Phys.* 74:041920.
14. Graham, B. P., K. Lauchlan, and D. R. McLean. 2006. Dynamics of outgrowth in a continuum model of neurite elongation. *J. Comput. Neurosci.* 20:43–60.
15. Hammele, M., and W. Zimmermann. 2003. Modeling oscillatory microtubule polymerization. *Phys. Rev. E Stat. Nonlin. Soft Matter Phys.* 67:021903.
16. Hentschel, H. G., and A. Fine. 1994. Instabilities in cellular dendritic morphogenesis. *Phys. Rev. Lett.* 73:3592–3595.
17. Hentschel, H. G., and A. Fine. 1996. Diffusion-regulated control of cellular dendritic morphogenesis. *Proc. Biol. Sci.* 263:1–8.
18. Janulevicius, A., J. van Pelt, and A. van Ooyen. 2006. Compartment volume influences microtubule dynamic instability: a model study. *Biophys. J.* 90:788–798.
19. Jobs, E., D. E. Wolf, and H. Flyvbjerg. 1997. Modeling microtubule oscillations. *Phys. Rev. Lett.* 79:519–522.
20. Li, G. -H., C. -d. Qin, and L. -W. Wang. 1995. Computer model of growth cone behavior and neuronal morphogenesis. *J. Theor. Biol.* 174:381–389.
21. McLean, D. R., and B. P. Graham. 2006. Stability in a mathematical model of neurite elongation. *Math. Med. Biol.* 23:101–117.
22. Miller, K. E., and D. C. Samuels. 1997. The axon as a metabolic compartment: protein degradation, transport, and maximum length of an axon. *J. Theor. Biol.* 186:373–379.
23. Alberts, P., R. Rudge, T. Irinopoulou, L. Danglot, C. Gauthier-Rouviere, et al. 2006. Cdc42 and actin control polarized expression of TI-VAMP vesicles to neuronal growth cones and their fusion with the plasma membrane. *Mol. Biol. Cell.* 17:1194–1203.
24. Martinez-Arca, S., P. Alberts, A. Zahraoui, D. Louvard, and T. Galli. 2000. Role of tetanus neurotoxin insensitive vesicle-associated membrane protein (TI-VAMP) in vesicular transport mediating neurite outgrowth. *J. Cell Biol.* 149:889–899.
25. Alberts, P., R. Rudge, I. Hinners, A. Muzerelle, S. Martinez-Arca, et al. 2003. Cross talk between tetanus neurotoxin-insensitive vesicle-associated membrane protein-mediated transport and L1-mediated adhesion. *Mol. Biol. Cell.* 14:4207–4220.
26. Lockerbie, R. O., V. E. Miller, and K. H. Pfenninger. 1991. Regulated plasmalemmal expansion in nerve growth cones. *J. Cell Biol.* 112:1215–1227.
27. Pfenninger, K. H., L. Laurino, D. Peretti, X. Wang, S. Rosso, et al. 2003. Regulation of membrane expansion at the nerve growth cone. *J. Cell Sci.* 116:1209–1217.
28. Shea, T. B., and V. S. Sapirstein. 1988. Vesicle-mediated delivery of membrane to growth cones during neuritogenesis in embryonic rat primary neuronal cultures. *Exp. Cell Biol.* 56:67–73.
29. Schmoranzer, J., G. Kreitzer, and S. M. Simon. 2003. Migrating fibroblasts perform polarized, microtubule-dependent exocytosis towards the leading edge. *J. Cell Sci.* 116:4513–4519.
30. Schmoranzer, J., and S. M. Simon. 2003. Role of microtubules in fusion of post-Golgi vesicles to the plasma membrane. *Mol. Biol. Cell.* 14:1558–1569.
31. Vega, I. E., and S. C. Hsu. 2001. The exocyst complex associates with microtubules to mediate vesicle targeting and neurite outgrowth. *J. Neurosci.* 21:3839–3848.
32. Zakharenko, S., and S. Popov. 1998. Dynamics of axonal microtubules regulate the topology of new membrane insertion into the growing neurites. *J. Cell Biol.* 143:1077–1086.
33. Grabham, P. W., B. Reznik, and D. J. Goldberg. 2003. Microtubule and Rac 1-dependent F-actin in growth cones. *J. Cell Sci.* 116:3739–3748.
34. Zhou, F. Q., C. M. Waterman-Storer, and C. S. Cohan. 2002. Focal loss of actin bundles causes microtubule redistribution and growth cone turning. *J. Cell Biol.* 157:839–849.
35. Prochiantz, A. 1995. Neuronal polarity: giving neurons heads and tails. *Neuron.* 15:743–746.
36. Ledesma, M. D., and C. G. Dotti. 2003. Membrane and cytoskeleton dynamics during axonal elongation and stabilization. *Int. Rev. Cytol.* 227:183–219.
37. Alberts, P., and T. Galli. 2003. The cell outgrowth secretory endosome (COSE): a specialized compartment involved in neuronal morphogenesis. *Biol. Cell.* 95:419–424.
38. de Anda, F. C., G. Pollarolo, J. S. Da Silva, P. G. Camoletto, F. Feiguin, et al. 2005. Centrosome localization determines neuronal polarity. *Nature.* 436:704–708.
39. Smith, C. L. 1994. The initiation of neurite outgrowth by sympathetic neurons grown in vitro does not depend on assembly of microtubules. *J. Cell Biol.* 127:1407–1418.
40. Silverman, M. A., S. Kaech, M. Jareb, M. A. Burack, L. Vogt, et al. 2001. Sorting and directed transport of membrane proteins during development of hippocampal neurons in culture. *Proc. Natl. Acad. Sci. USA.* 98:7051–7057.
41. Horton, A. C., B. Racz, E. E. Monson, A. L. Lin, R. J. Weinberg, et al. 2005. Polarized secretory trafficking directs cargo for asymmetric dendrite growth and morphogenesis. *Neuron.* 48:757–771.
42. Holcman, D., and Z. Schuss. 2004. Escape through a small opening: receptor trafficking in a synaptic membrane. *J. Stat. Phys.* V117: 975–1014.
43. Schuss, Z. 1980. Theory and Applications of Stochastic Differential Equations. J. Wiley, New York.
44. Han, W., Y. K. Ng, D. Axelrod, and E. S. Levitan. 1999. Neuropeptide release by efficient recruitment of diffusing cytoplasmic secretory vesicles. *Proc. Natl. Acad. Sci. USA.* 96:14577–14582.
45. Hill, D. B., M. J. Plaza, K. Bonin, and G. Holzwarth. 2004. Fast vesicle transport in PC12 neurites: velocities and forces. *Eur. Biophys. J.* 33:623–632.
46. Singer, A., and Z. Schuss. 2006. Activation through a narrow opening. *Phys. Rev. E Stat. Nonlin. Soft Matter Phys.* 74:020103–020104.
47. Nishimura, T., Y. Fukata, K. Kato, T. Yamaguchi, Y. Matsuura, et al. 2003. CRMP-2 regulates polarized Numb-mediated endocytosis for axon growth. *Nat. Cell Biol.* 5:819–826.
48. Schuss, Z., A. Singer, and D. Holcman. 2007. The narrow escape problem for diffusion in cellular microdomains. *Proc. Natl. Acad. Sci. USA.* 104:16098–16103.
49. Slepchenko, B. M., I. Semenova, I. Zaliapin, and V. Rodionov. 2007. Switching of membrane organelles between cytoskeletal transport systems is determined by regulation of the microtubule-based transport. *J. Cell Biol.* 179:635–641.
50. Nakata, T., and N. Hirokawa. 2007. Neuronal polarity and the kinesin superfamily proteins. *Sci. STKE.* 2007:pe6.
51. Fournier, A. E., F. Nakamura, S. Kawamoto, Y. Goshima, R. G. Kalb, et al. 2000. Semaphorin3A enhances endocytosis at sites of

receptor-F-actin colocalization during growth cone collapse. *J. Cell Biol.* 149:411–422.

52. Jurney, W. M., G. Gallo, P. C. Letourneau, and S. C. McLoon. 2002. Rac1-mediated endocytosis during ephrin-A2- and semaphorin 3A-induced growth cone collapse. *J. Neurosci.* 22:6019–6028.
53. Craig, A. M., R. J. Wyborski, and G. Banker. 1995. Preferential addition of newly synthesized membrane protein at axonal growth cones. *Nature.* 375:592–594.
54. Howard, J., and A. A. Hyman. 2003. Dynamics and mechanics of the microtubule plus end. *Nature.* 422:753–758.
55. Diefenbach, T. J., P. B. Guthrie, H. Stier, B. Billups, and S. B. Kater. 1999. Membrane recycling in the neuronal growth cone revealed by FM1–43 labeling. *J. Neurosci.* 19:9436–9444.
56. Mehta, S. Q., P. R. Hiesinger, S. Beronja, R. G. Zhai, K. L. Schulze, et al. 2005. Mutations in *Drosophila* sec15 reveal a function in neuronal targeting for a subset of exocyst components. *Neuron.* 46:219–232.
57. Murthy, M., D. Garza, R. H. Scheller, and T. L. Schwarz. 2003. Mutations in the exocyst component Sec5 disrupt neuronal membrane traffic, but neurotransmitter release persists. *Neuron.* 37:433–447.
58. Dickson, B. J. 2002. Molecular mechanisms of axon guidance. *Science.* 298:1959–1964.
59. Kalil, K., and E. W. Dent. 2005. Touch and go: guidance cues signal to the growth cone cytoskeleton. *Curr. Opin. Neurobiol.* 15:521–526.
60. Dotti, C. G., C. A. Sullivan, and G. A. Banker. 1988. The establishment of polarity by hippocampal neurons in culture. *J. Neurosci.* 8:1454–1468.
61. Matteoli, M., K. Takei, M. S. Perin, T. C. Sudhof, and P. De Camilli. 1992. Exo-endocytotic recycling of synaptic vesicles in developing processes of cultured hippocampal neurons. *J. Cell Biol.* 117:849–861.
62. Tanaka, E., and J. Sabry. 1995. Making the connection: cytoskeletal rearrangements during growth cone guidance. *Cell.* 83:171–176.
63. Erck, C., L. Peris, A. Andrieux, C. Meissirel, A. D. Gruber, et al. 2005. A vital role of tubulin-tyrosine-ligase for neuronal organization. *Proc. Natl. Acad. Sci. USA.* 102:7853–7858.
64. Witte, H., D. Neukirchen, and F. Bradke. 2008. Microtubule stabilization specifies initial neuronal polarization. *J. Cell Biol.* 180:619–632.
65. Cole, R. A., and J. E. Fowler. 2006. Polarized growth: maintaining focus on the tip. *Curr. Opin. Plant Biol.* 9:579–588.
66. Samaj, J., J. Muller, M. Beck, N. Bohm, and D. Menzel. 2006. Vesicular trafficking, cytoskeleton and signaling in root hairs and pollen tubes. *Trends Plant Sci.* 11:594–600.
67. Steinberg, G. 2007. Hyphal growth: a tale of motors, lipids, and the Spitzenkorper. *Eukaryot. Cell.* 6:351–360.
68. Burbank, K. S., and T. J. Mitchison. 2006. Microtubule dynamic instability. *Curr. Biol.* 16:R516–R517.
69. Kerssemakers, J. W., E. L. Munteanu, L. Laan, T. L. Noetzel, M. E. Janson, et al. 2006. Assembly dynamics of microtubules at molecular resolution. *Nature.* 442:709–712.